Proceedings of the Design Society, Volume 5: ICED25
https://doi.org/10.1017/pds.2025.10115

Computational analysis of overhang surface roughness effects on self-supporting channels

Alexander Seidler✉, Stefan Holtzhausen and Kristin Paetzold-Byhain

Technical University Dresden, Germany

✉ alexander.seidler@tu-dresden.de

ABSTRACT: Additive manufacturing (AM) enables the creation of complex internal geometries, including cooling channels. Yet, the impact of AM-induced surface roughness on their fluid dynamics remains underexplored. The goal of this study is to provide insight into the effects of surface roughness on the fluid dynamics of AM channels. A parametric surface roughness model and computational fluid dynamics (CFD) simulations were employed to examine three representative AM channel cross-sections: diamond, droplet, and circular. The findings indicate that diamond profiles result in higher pressure losses and turbulence intensity compared to the other cross-sections. In contrast, droplet profiles exhibit lower pressure losses and turbulence intensity compared to diamond profiles, while circular channels remain optimal in non-overhang areas.

KEYWORDS: additive manufacturing, design for additive manufacturing (DfAM), simulation, flow components, surface roughness

1. Introduction

The design limitations of complex internal structures are almost entirely resolved with additive manufacturing (AM). AM enables mass optimization through topology-optimized or cellular designs, reducing weight while maintaining stiffness. Metallic AM technologies like Laser Powder Bed Fusion (LPBF) facilitate internal cooling channels for energy transport, benefiting applications such as heat exchangers and mold or tool making (Zhang et al., 2020). Current research on conformal cooling channels focuses on organic, small-diameter channel design (Lamarche-Gagnon et al., 2024). The aim is to diminish the distance between the cooling channel and the heat-loaded surface while augmenting the channel length to expand the heat-transferring wall area. Fulfilling this optimization enhances the compactness and energy efficiency of the cooling structure, whereby LPBF is identified as the optimal process for the manufacture of such optimized metallic components. In this process, the components are created layer by layer through the selective melting of metal powder using a laser as heat source (Kasperovich et al., 2021). However, the manufacturing of component surfaces with an inclination of less than 30° relative to the build plate (downskin surfaces in the overhang) is not feasible (Han et al., 2018) and represents a significant challenge in this process. The restricted transfer of heat during the manufacturing of components with an overhang results in an increase in the level of roughness and manufacturing inconsistencies (Bulsiewicz & Łapka, 2024; Kasperovich et al., 2021). These limitations also extend to AM cooling channel structures with diameters (d) in the micro- and mesoscale range ($d < 10$ mm), as substantial surface irregularities can markedly diminish or even entirely occlude the effective cross-sectional area, leading to a loss of functionality in the channel structures (Kasperovich et al., 2021). It has been demonstrated that the cross-section of the circular channel lacks the capacity for self-support, resulting in an increased surface roughness (Kasperovich et al., 2021). In order to address the aforementioned challenges, alternative self-supporting channel cross-sections have been developed and investigated to improve the surface quality and manufacturing accuracy of channel structures (Biedermann & Meboldt, 2020). Research in Design for Additive Manufacturing (DfAM) has primarily

https://doi.org/10.1017/pds.2025.10115 Published online by Cambridge University Press

focused on developing AM channels with diamond and droplet cross-sections. (Biedermann et al., 2022a). This focus is driven by ISO/ASTM 52911-1:2020-05, which recommends droplet cross-sections as an alternative to circular cross-sections in overhang areas (F42 Committee; Tappeiner et al., 2024). Additionally, Schmelzle et al. (2015) demonstrated that diamond cross-sections offer superior mechanical strength under loading compared to droplet cross-sections. Consequently, this study focuses on these two self-supporting cross-section designs. However, the impact of manufacturing-induced surface roughness on the fluid-dynamic behavior of these AM channel geometries at the micro- and mesoscale remains largely unexplored, highlighting the need for further research. A comprehensive understanding of this behavior is crucial for identifying opportunities for geometric optimization and enhancing the performance of AM channels (Biedermann et al., 2022b; Hartsfield et al., 2021).

In previous studies on the fluid-dynamic analysis of channel structures, the surface roughness was frequently represented in a simplified manner by constant roughness values (Schmitt et al., 2023; Tappeiner et al., 2024). Additionally, the roughness modeling of channels often employs roughness data of planar AM surfaces, which may not fully capture the intricacies of the surface topography and its dependency on the overhang of surfaces (Garg et al., 2023). Several studies highlight the necessity for a more comprehensive analysis considering the specific roughness profiles of additively manufactured surfaces (Biedermann et al., 2022b; Garg et al., 2023; Tappeiner et al., 2024). In order to address this need, one of the primary research objectives of the DfAM investigation is the precise modeling of the topography of surfaces produced by LPBF. The development of implicit modeling approaches has facilitated the realization of new possibilities for the accurate mapping of the intricate roughness profiles of additively manufactured structures. In this context, a parametric model for the synthesis of AM surface topography in LPBF-manufactured lattice structures was proposed (Chahid et al., 2021). The approach is based on an implicit field-based model, which was realized using a field with simplex noise, a function that generates smooth gradient-based noise patterns (Perlin, 2002), within the software ***nTop*** (nTop Inc.). This approach was successfully employed to model the surface roughness of lattice beams to determine the mechanical effects of surface topography. However, the presented model is only partially suitable for modeling the surface topography of channel structures, as the heterogeneity of the varying surface topographies is differentiated in binary upskin-downskin, resulting in a significant simplification of the geometric resolution of the surface topography depending on the overhang angle. The goal of this study is to analyze common self-supporting cross-sectional designs for AM channels by examining their fluid dynamic behavior in the presence of modelled manufacturing-induced surface roughness through the use of computational fluid dynamics (CFD) simulations. To accomplish this, an enhanced modeling approach, based on the work of Chahid et al. (2021), has been developed to more accurately replicate the heterogeneous surface topography of AM channels fabricated via LPBF. This model is used to generate synthetic geometry data for various channel designs, including self-supporting (diamond, droplet) and non-self-supporting (circular) profiles.

2. Material and methods

2.1. Parametrical model for AM surface topography synthesis

Parametrical model for surface topography of AM channels

Building upon the work of Chahid et al. (2021), the simplex noise approach for the parametric description of surface topographies has been further developed to enable an angle-dependent definition of roughness as a function of the overhang angle (φ). The objective is to achieve a consistent geometric description in which different roughness fields can be seamlessly transformed into one another. The foundation of this approach is an angular field (**S**φ) as defined below (Equation 1), which describes the angle of surface orientation about the build direction (Z+) for each position on the geometry (Ω) (Figure 1, left). The angle field is employed to segment the geometry into n areas, thereby ensuring the accuracy of the synthetic AM surface topography mapping. For each of these areas, a noise field is parameterized by a frequency (f). The quantity f is unitless and indicates the density of roughness. The simplex noise field is multiplied by the amplitude $\hat{a}$, whereas this quantity is the maximum surface deviation. This operation generates a signed distance field (SDF) that describes the local surface deviation as a roughness field ($\mathbf{S}_{\mathrm{Ri}}$) relative to the ideal geometry (Figure 1 right). In order to achieve a smooth transition between the various roughness

https://doi.org/10.1017/pds.2025.10115 Published online by Cambridge University Press

fields, an angle-dependent blending factor (w) is introduced by (Equation 2). The SDF of total surface roughness ($\mathbf{S}_\mathrm{R}$) of the component is ultimately derived by the summation of the individual roughness fields ($\mathbf{S}_{\mathrm{Ri}}$), as outlined in (Equation 3). The integration of the surface roughness with the geometry model is achieved adding the SDF of the geometry ($\mathbf{S}_\Omega$) and the total roughness ($\mathbf{S}_\mathrm{R}$). This model was implemented using the software ***nTop*** (nTop Inc.). Consequently, this approach allows for the application of surface roughness to geometries in a scalable manner.

$$S\,\varphi(x,y,z) = \mathrm{atan2}\left(\frac{x}{y}\right)\cdot\frac{180^\circ}{2\cdot\pi}\cdot n_{-z} \tag{1}$$

$$w(\,\varphi) = \begin{cases} \frac{S_\varphi}{\varphi_{i-1}}, 0^\circ \le \varphi \le \varphi_{i-1} \\ \frac{S_\varphi - \varphi_{i-1}}{\varphi_i - \varphi_{i-1}},\ \varphi_{i-1} \le \varphi \le \varphi_i \\ \frac{S_\varphi - \varphi_0}{\varphi_0 - \varphi_i},\ \varphi_i \le \varphi \le \varphi_0 \end{cases} \tag{2}$$

$$S_R(\,\varphi) = \widehat{a}_0 \cdot N_0(f_0) + \begin{cases} (1-w)\cdot\widehat{a}_1\cdot N_1(f_1) + \widehat{a}_{\mathrm{i}-1}\cdot \mathrm{w}\cdot N_{\mathrm{i}-1}(f_{\mathrm{i}-1}), 0^\circ \le \varphi \le \varphi_{i-1} \\ (1-\mathrm{w})\cdot\widehat{a}_{\mathrm{i}-1}\cdot N_{\mathrm{i}-1}(f_{\mathrm{i}-1}) + \widehat{a}_{\mathrm{i}}\cdot \mathrm{w}\cdot N_{\mathrm{i}}(f_{\mathrm{i}}),\ \varphi_{i-1} \le \varphi \le \varphi_i \\ (1-\mathrm{w})\cdot\widehat{a}_{\mathrm{i}}\cdot N_{\mathrm{i}}(f_{\mathrm{i}}),\ \varphi_i \le \varphi \le \varphi_0 \end{cases} \tag{3}$$

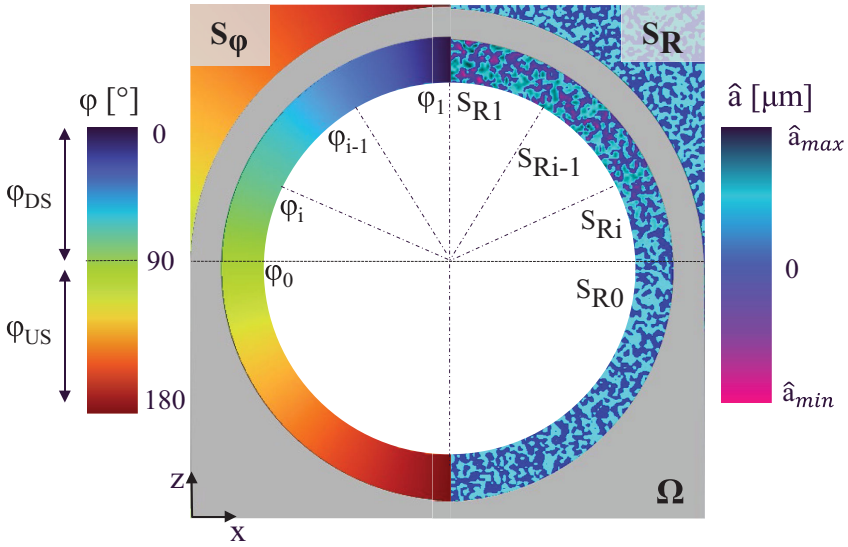


Figure 1. Field-driven synthesis of manufacturing angle-dependent surface roughness

Calibration of surface topography model for circular AM channels

The surface model for circular AM channels (Sec. 2.1) was calibrated using roughness measurements of AM channels in the overhang area ($\varphi < 90^\circ$) carried out by Han et al. (2018). A quantitative comparison of the measurement results with the modeled roughness at measuring points III-V was conducted using the average Roughness (Ra). For the characterization of the topography, five angular ranges were defined (Table 1). No surface roughness measurements were carried out in the downskin range (φ1), corresponding to an overhang angle (φ) of 0°. Accordingly, the parameters for frequency and amplitude of surface roughness from Chahid et al. (2021) were employed. This also applies to the upskin area ($\varphi > 90^\circ$; Table 1). The measuring points I and II defined by Han et al. (2018) were defined in a simplified manner as upskin areas. For measurement locations III-V (Han et al., 2018), the amplitudes were determined based on the maximum deviations of the respective measurement location and the frequencies were calculated by linear interpolation between the frequencies of the angular zones φ0 and φ1. Correction factors were introduced to precisely adjust the amplitudes in the III-V ranges, aiming to achieve equivalent Ra values for the measurement ranges. These adjustments are essential due to the inherent nature of the noise function, which is based on a normal distribution, thereby generating values

https://doi.org/10.1017/pds.2025.10115 Published online by Cambridge University Press

between -1 and 1. Given that the probability of maximum and minimum values occurring is low, it is necessary to apply corrections to ensure that the modeled amplitude is aligned with the actual amplitude to be mapped.

Table 1. Parameter for synthesize a circular AM channel surface roughness

ϕ	i	f_i	$\hat{a}_i[\mu m]$
0°	1	1850	315
φ_V= 45°	2	2140	210
φ_{IV} = 60°	3	2220	180
φ_{III} = 90°	4	2405	15
90° 180°	0	2960	10

Roughness evaluation

In order to align the data on surface roughness generated through synthesis with the empirical findings of Han et al. (2018), an algorithm was devised to quantify the surface roughness along a designated measurement line positioned on the idealized geometric surface. The geometry (Ω) with a rough modeled surface is discretized by a three-dimensional surface mesh. The measurement points ($\mathbf{p}_i$) are distributed uniformly along the measuring line. The number of measurement points is calculated in accordance with the Nyquist-Shannon sampling theorem, whereby the maximum frequency (f_{max}) is derived from two times of f_0 (Table 1). This results in approximately 6,000 measuring points along the line (4 mm). Subsequently, the shortest distance between the measuring point on the line and the nearest mesh point on the surface is determined. By the geometric surface roughness model presented in Section 2.1, the identified parameters (Table 1) were evaluated based on the findings by Han et al. (2018). The surface deviations on the synthetic geometry model (Figure 2a) are further compared with the measurements presented in Figure 2b.

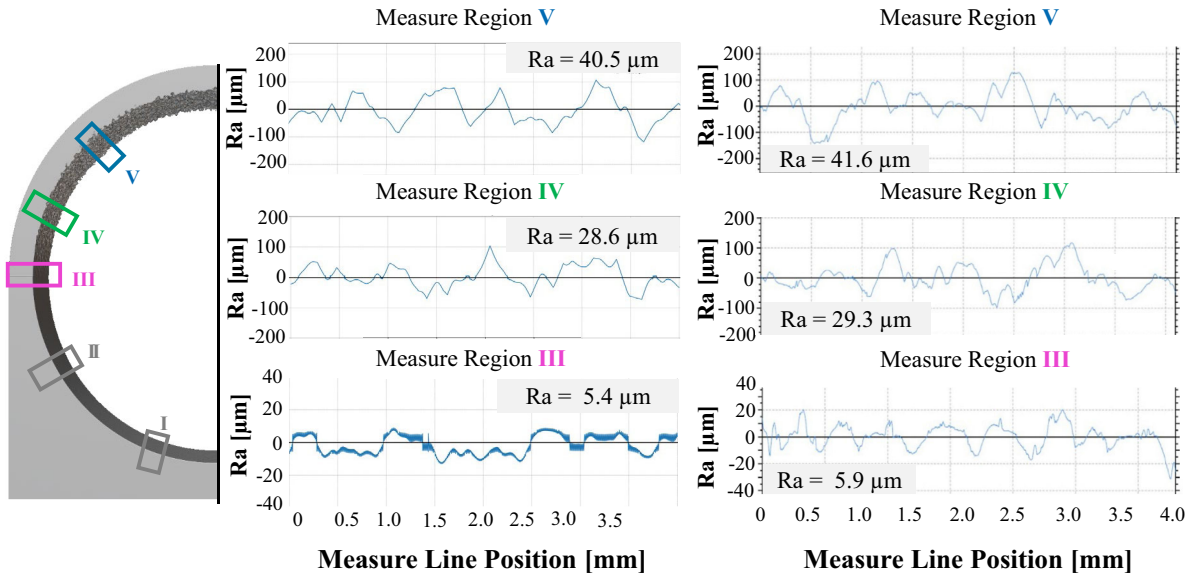


Figure 2. Surface roughness of a pipe section measured at three locations for a) modeled surface roughness and b) measured surface roughness on an AM pipe section (Han et al., 2018)

The AM surface roughness synthesis model was adjusted using experimentally determined Ra values, demonstrating a strong correlation with the measured data. The most significant discrepancy of approximately 9%, was observed at location III (Figure 2a Region III). This can be attributed to the limited precision inherent in the discretization techniques employed for minor roughness features. At Regions IV and V (Figure 2a), discrepancies were approximately 3%, with the roughness curves exhibiting a high degree of qualitative alignment with the measurements (Figure 2b). The discrepancies

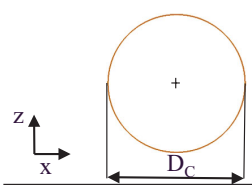
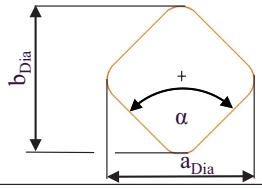
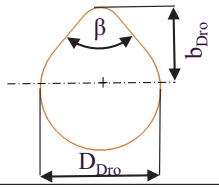
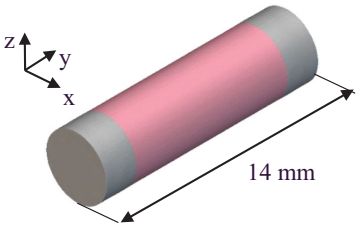
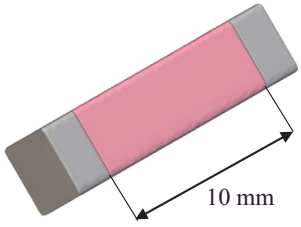
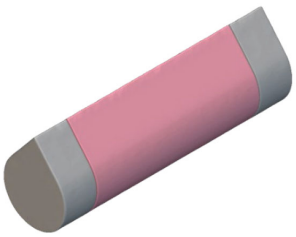
https://doi.org/10.1017/pds.2025.10115 Published online by Cambridge University Press

observed at the most minor scales are a consequence of the inherent limitations of the discretization process. Nevertheless, the presented approach for surface roughness modeling (Section 2.1) indicates to generate highly detailed AM surface roughness with an accurate representation of the measured data, thus providing a foundation for further fluid dynamics analyses of AM channels.

2.2. Fluid model synthesis of AM channels

In order to investigate the effect of manufacturing-related surface roughness on fluid flow in AM channels (Ch), three different cross-sectional geometries were subjected to analysis. The three geometries were designated with a circle (CiCh), diamond (DiCh), and droplet (DrCh) cross-sectional surface geometry (Table 2). To improve the interpolation of the roughness model scaled to circular cross-sections, the corners of the diamond and droplet cross-sections were rounded for this investigation. In order to conduct a Computational Fluid Dynamics (CFD), the fluid volume within the channel structures must be modeled. The three AM channels are 14 mm long and have a constant cross-sectional area of 12.57 mm^2. The diameter of the circular cross-section (CiCh) is 4 millimeters. The manufacturing-related surface roughness was modeled over a length of 10 mm (Table 2, highlighted in red). The inlet and outlet areas were simplified to ensure defined initial boundary conditions for the CFD analyses. The fluid volumes are aligned in the direction of the AM channel, so that the fluid flow takes place along the Y-axis and the cross-sectional geometries are defined in the X-Z plane.

Table 2. Parameter for fluid geometry of different AM channels

CiCh	DiCh	DrCh
		
Dc = 4 mm A_{Circ} = 12.57 mm² C_{Circ} = 12.56 mm	$a_{Dia} = b_{Dia}$ = 4.8 mm $\alpha = 45°$ A_{Diam} = 12.54 mm² C_{Diam} = 13.70 mm	b_{Drop} = 2.87 mm; D_{Drop} = 3.8 mm; $\beta = 50°$ A_{Drop} = 12.54 mm² C_{Drop} = 13.07 mm
		

Surface roughness integration in AM channel fluid models

The synthesis of AM channel geometries, incorporating manufacturing-induced surface roughness, is based on the initial geometries detailed in Table 2. The surface roughness for each fluid volume was generated by the respective angular field, with parameters derived from the adjusted model of the circular AM channel (Table 1). The fluid volumes with surface roughness taken into account show different maximum surface deviations (Figure 3).

The highest surface roughness, approximately 300 µm, is observed in the rough circular channel ($CiCh_R$), which can be attributed to overhang angles below 30°. The Droplet Channel ($DrCh_R$) models exhibit the lowest surface deviations, at approximately 150 µm, due to the profile angle β = 50° (Table 2). In contrast, the maximum deviations for the diamond channel ($DiCh_R$) are linked to the profile angle α = 45°, reaching approximately 240 µm.

https://doi.org/10.1017/pds.2025.10115 Published online by Cambridge University Press

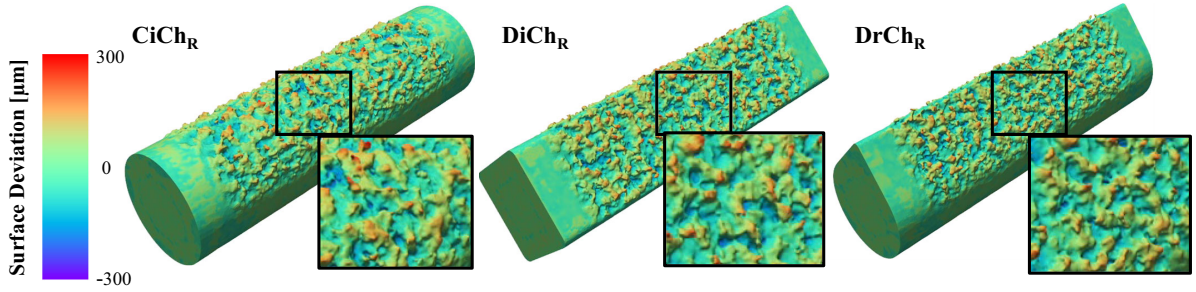


Figure 3. Fluid design of AM channels considering overhang-adapted surface roughness

Limitations

This study analyzes the impact of surface roughness on the fluid dynamics of various AM channel geometries. The surface roughness model presented herein focuses exclusively on the relative orientation of geometric elements with respect to the build plate for LPBF-manufactured parts, neglecting considerations of thermal effects and heat transfer phenomena in self-supporting geometries. Moreover, the surface roughness data for diamond and droplet channel structures were extrapolated from circular channel data, which likely leads to an overestimation of roughness in overhang areas due to these limitations.

2.3. CFD-analysis

Simulation setup

CFD simulations were conducted using Ansys® ANSYS FLUENT 2024R1 (Ansys Inc.) to analyze the fluid dynamic behavior. The fluid assumed was water at 20 °C with a density of $\rho = 998\ kg/m^3$ and a kinetic viscosity of $\nu = 1.0034 \times 10^{-6}\ m^2/s$. The fluid behavior is analyzed with regard to both laminar and turbulent flow behavior. Accordingly, two distinct simulation models are required to map the laminar and turbulent flow behaviors. The Shear Stress Transport (SST) k-ω turbulence model is employed to simulate turbulent flow. It is assumed that the fluid behavior is steady-state for the purposes of the flow simulations. The three geometries ($CiCh_R$, $DiCh_R$, $DrCh_R$) are examined under the same Reynolds numbers (Re) for fully-developed laminar and turbulent flow conditions. In accordance with the Reynolds number, the mean flow velocity (u_{mean}) at the inlet is calculated (Equation 10) for the various geometries. By (Equation 11), the hydraulic diameter (D_H) is calculated for all AM channels. The hydraulic diameter (D_H) is defined as the ratio of the cross-sectional area (A) of a given geometry to its wetted perimeter (C). In order to ensure that the pipe flows are fully developed, the hydraulic inlet lengths (L_E) for laminar (L_E = 247 mm) and turbulent flows (L_E = 79 mm) were calculated with (Equation 12). By the aforementioned criteria, pipes with a length of 300 mm are defined for laminar flows and 100 mm for turbulent flows. The inlet boundary conditions were about the smooth channel models (CiCh, DiCh, DrCh). In this instance, the profile-dependent mean velocity was applied to the entire inlet surface. Furthermore, the flow profiles of the fully developed pipe flow at the outlet were stored as user-defined functions (UDF) and subsequently employed as inlet conditions to simulate the rough AM channels (Table 3). The turbulence intensity (I_{turb}) at the inlet was estimated according to (Equation 13) for Re=8000, resulting in an estimated value of approximately 5%, which is a realistic assumption for internal pipe flows.

$$Re = \frac{u_{mean} * D_H}{\nu} \tag{10}$$

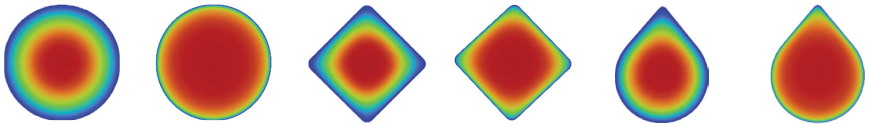
$$D_H = 4 \cdot \mathrm{A} \cdot \mathrm{C}^{-1} \tag{11}$$

$$L_E = \begin{cases} D_H \cdot 0.06 \cdot Re; Re \leq 2300 \\ D_H \cdot 4.4 \cdot Re^{1/6}; Re > 4000 \end{cases} \tag{12}$$

$$I_{turb} = 0.16 \cdot Re^{-1/8} \tag{13}$$

https://doi.org/10.1017/pds.2025.10115 Published online by Cambridge University Press

Table 3. Boundary conditions of the simulation models

	$CiCh_R$		$DiCh_R$		$DrCh_R$	
Wall	No Slip					
Outlet Pressure [Pa]	0					
Re	1000	8000	1000	8000	1000	8000
D_H [mm]	4		3.66		3.84	
u_{mean} [m/s]	0.2508	2.007	0.274	2.19	0.261	2.09
Qualitative Velocity Profile						

A pressure-based solver with absolute velocity formulation and double precision solves the equations using a coupled pressure-velocity algorithm and second-order upwind schemes for momentum, pressure, turbulent kinetic energy, and specific dissipation rate.

Mesh

The superior cell orthogonality of polyhedral elements compared to tetrahedral elements leads to their utilization for the simulation mesh, which facilitates enhanced gradient resolution and augments the precision of the simulation. For the first boundary layer, an initial cell height of 0.001 mm was selected to model the intricate surface layer structure (Figure 3), corresponding to a y+ value of 0.17, which is below the threshold for wall model requirements (y+ > 30). In order to maintain a constant first boundary layer height, the near-wall region is resolved with 20 boundary layers. The maximum permitted cell size is 0.1 mm, with a growth rate of 1.1.to ascertain the precision of the AM channels' discretization a mesh convergence study is conducted at $CiCh_R$ (Figure 3). The pressure loss deviation for laminar flows is used as a reference. A mesh convergence study utilized three meshes: $Mesh_1$ (14,983,577 elements), $Mesh_2$ (27,032,718 elements), and $Mesh_3$ (44,192,885 elements). The pressure losses deviate by 3.3% between $Mesh_1$ and $Mesh_2$, and by 1.7% between $Mesh_2$ and $Mesh_3$. A 1.7% deviation confirms the adequacy of $Mesh_2$ for accurate pressure loss calculations. However, to capture the highly complex AM surface topography ~44 million polyhedral cells per geometry were employed in the simulations.

Analytical evaluation

In addition to the mesh convergence study, the laminar and turbulent simulation models are subjected to a physical accuracy evaluation. The Darcy-Weisbach (Equation 14) is employed for the evaluation. The initial geometry CiCh (Table 2) is employed for the analytical validation. The boundary conditions specified in Table 3 are employed in the simulations of both laminar and turbulent flows. A comparison is made between the simulation and the analytical formula, with the pressure loss (Δp) according to (Equation 14) being compared with the simulation results. The friction loss factor (f) is calculated using the Swamee-approximation (Swamee, 1993) (Equation 15) of the implicit Colebrook equation.

$$\Delta p = f \cdot \frac{L \cdot \rho \cdot v^2}{2 \cdot D_H} \tag{14}$$

$$f = \left(\left(\frac{64}{Re} \right)^8 + 9.5 \cdot \left(\ln \left(\frac{\varepsilon}{3.7 \cdot D_H} + \frac{5.74}{Re^{0.9}} \right) - \left(\frac{2500}{Re} \right)^6 \right)^{-16} \right)^{1/8} \tag{15}$$

In the Swamee approximation, the parameter ε represents pipe wall roughness, with $\varepsilon = 0$ validating smooth pipes analytically. The CFD model calculated a pressure loss of 7.08 Pa for CiCh, differing by 0.77% from the analytical solution. Using the turbulent SST-k-ω model, the pressure loss for CiCh was 197.68 Pa, approximately 14% lower than the analytical equation. These discrepancies stem from the Swamee approximation's accuracy of approximately 2.8% (Brkić, 2011) and the empirical nature of the Darcy-Weisbach equation. Additionally, ideal smooth walls as simulation boundary conditions contribute to deviations. Given the different approaches to turbulent flow modeling, a 14% discrepancy is within an acceptable margin.

https://doi.org/10.1017/pds.2025.10115 Published online by Cambridge University Press

3. Results and Discussion

Pressure loss

A series of simulations were conducted to determine pressure losses in rough channel structures over a 10 mm length, excluding the 2 mm smooth-wall regions at the inlet and outlet (Table 2, highlighted in red), under both laminar and turbulent flow conditions. For laminar flow, the pressure loss for $DiCh_R$ is highest at 6.89 Pa, while $CiCh_R$ exhibits the lowest pressure loss at 5.34 Pa. $DrCh_R$ shows an intermediate pressure loss at 6.00 Pa. For turbulent flows (Re = 8000), $DiCh_R$ demonstrates the most significant pressure loss at 219.1 Pa, with $DrCh_R$ exhibiting a comparatively lower value of 194.1 Pa. In contrast, $CiCh_R$ exhibits the lowest pressure loss at 178.8 Pa.

The comparative analysis reveals that in laminar flow, pressure loss is 29.0% higher for $DiCh_R$ and 12.3% higher for $DrCh_R$ compared to $CiCh_R$. In turbulent flow, the discrepancy in pressure loss between $DiCh_R$ and $CiCh_R$ decreases to 22.5%, with a reduction of 6.5 percentage points compared to laminar flow conditions. The pressure loss for $DrCh_R$ in turbulent flow is 8.6% greater than $CiCh_R$, with a decrease in pressure loss deviation by 3.7 percentage points compared to laminar flow conditions. These findings suggest that laminar flows accentuate the impact of profile geometry on pressure loss in AM channels, whereas turbulent flow emphasizes the influence of surface roughness. As Re increases, the influence of surface roughness on pressure loss becomes more pronounced, resulting in a reduction in the gradient of pressure lossess of the self-supporting channel designs. This trend is due to the higher surface roughness of $CiCh_R$ in comparison to both $DiCh_R$ and $DrCh_R$ (Figure 3). Moreover, the pressure loss is inversely proportional to the hydraulic diameter: a larger circumference increases the friction, resulting in greater pressure loss. Consequently, $DiCh_R$ exhibits a higher lateral surface area leading to a higher pressure loss than $DrCh_R$ and $CiCh_R$.

To ensure the validity of the simulation results, the friction loss factor (f) for Re = 8000 is used for validation instead of the pressure loss, as proposed by Wildgoose and Thole (2023). This ensures comparability between studies with different experimental setups and channel designs. f is calculated (Equation 14) and scaled with the Re (Equation 10), where the square root of the cross-sectional area ($\sqrt{A}$) replaces the hydraulic diameter (D_H). Based on the simulated pressure losses, the unitless scaled friction factors ($f \cdot Re_{\sqrt{A}}$) are calculated for all channels:

$$f_{\mathrm{CiChR}} \cdot Re_{\sqrt{A}} = 252.2, f_{\mathrm{DiChR}} \cdot Re_{\sqrt{A}} = 258.8, f_{\mathrm{DrChR}} \cdot Re_{\sqrt{A}} = 252.1.$$

A Comparison of $f \cdot \mathrm{Re}_{\sqrt{A}}$ with experimental data from Wildgoose and Thole (2023) on AM microchannels reveals a deviation of ~ 30% for circular and diamond channels. The observed deviations are largely influenced by the L/D_H ratio, which is 10 times larger in the study of Wildgoose and Thole (2023) than in this work. Their setup examined fully developed flow, whereas this study only enforced it at the inlet under smooth wall flow conditions. Increasing the L/D_H ratio by extending L or reducing D_H would improve simulation accuracy. However, a comparison of friction loss factors between smooth and rough channels in the study of Wildgoose and Thole (2023) shows a 40% deviation. Yet, under the conditions of this study, this deviation is reduced by 9.6 percentage points for circular cross-sections and 12.5 percentage points for diamond cross-sections.

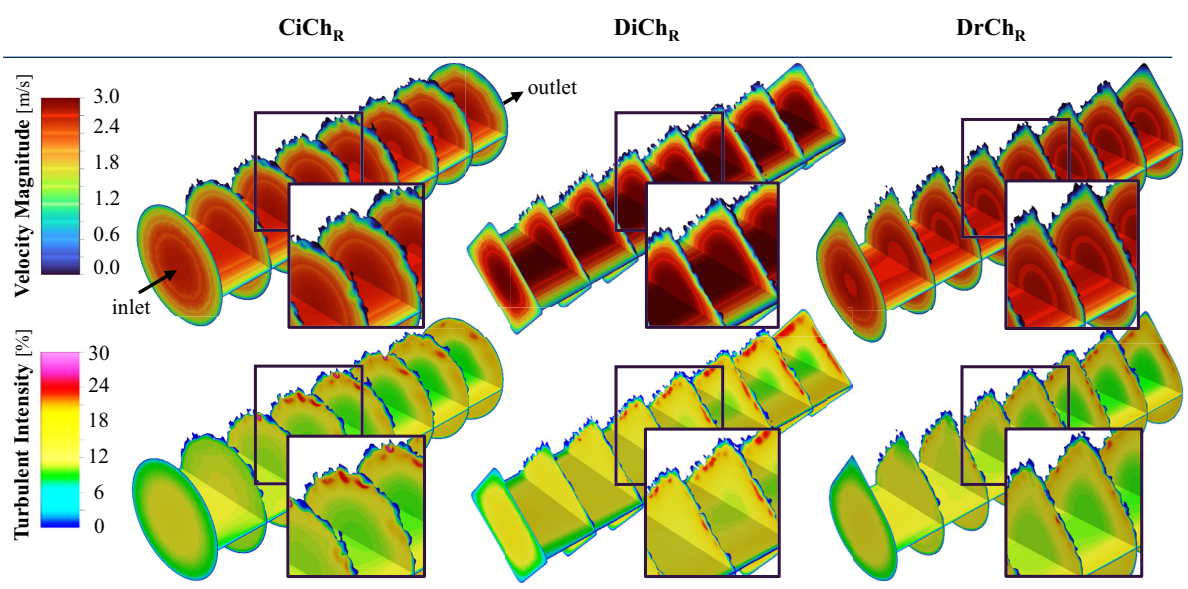
Fluid dynamical behaviour

The fluid-dynamic behavior was analyzed by determining pressure losses and also by observing the flow velocity and turbulence intensity (TI), which describes the ratio of velocity fluctuation to mean velocity (Table 4). The maximum velocity of 3.3 m/s is observed in $DiCh_R$, while the maximum velocity in $CiCh_R$ is lower at 2.67 m/s and in $DrCh_R$ at 2.9 m/s. These disparate velocities results from several factors, including the varying hydraulic diameters of the geometries and the effective channel cross-section's reduction due to surface roughness. As evidenced by the velocity fields presented in Table 4 the turbulent flow conditions in the AM channels demonstrate that the influence of increasing roughness in the overhang area results in a corresponding increase in the flow velocity. The high surface roughness at $CiCh_R$ results in the formation of a distinct boundary layer in comparison to the inlet. Furthermore, the mean flow profile over a shorter channel length is more homogeneous for $DrCh_R$ and $CiCh_R$ than for

https://doi.org/10.1017/pds.2025.10115 Published online by Cambridge University Press

$DiCh_R$. Additionally, dead water zones form at the corners of the cross-section at $DiCh_R$ and $DrCh_R$, which is consistent with the findings of Tappeiner et al. (2024).
The turbulent intensity fields (Table 4) reveal that geometry-induced turbulence develops in the overhang region ($\varphi < 90°$). These fields show mutual influence along the channel length, forming more heterogeneous high-turbulence zones (TI > 20%) at the outlet than at the inlet. The highest turbulence intensity (TI ~30%) is observed in the $CiCh_R$, due to its enhanced surface roughness compared to the $DiCh_R$ and $DrCh_R$. $DiCh_R$ and $DrCh_R$, with dead water zones in their corners and minimal overhang angles, show little increase in turbulence intensity despite higher surface roughness. However, $DiCh_R$ exhibits larger regions with TI > 20%, indicating higher overall turbulence. The asymmetric $DrCh_R$ has fewer turbulent zones than the symmetrical $DiCh_R$ due to its smaller lateral surface area in the critical overhang region. In contrast, $CiCh_R$ has dominant overhang areas ($\varphi < 30°$) contributing to high TI. While $DiCh_R$ has a rougher half-shell with lower roughness amplitudes, it tends to form flat, high-TI zones that intensify along the channel. $DrCh_R$ exhibits the least turbulence amplification, mainly due to lower surface roughness amplitudes and no noticeable TI enhancement along the channel.

Table 4. Fluid behaviour of AM channel for turbulent flow



The results of this simulation-based investigation of the fluid dynamics of self-supporting (diamond and droplet) and non-self-supporting (circular) cross-sections for AM channels led to several key findings. As the Reynolds number increases from 1000 to 8000, surface roughness becomes more dominant than profile geometry, emphasizing the need to consider surface conditions and roughness in AM channels under turbulent flow. For low pressure loss applications in overhang regions, droplet cross-sections are preferred due to their lower turbulence intensity and asymmetrical shape. Diamond cross-sections, with higher pressure losses and larger turbulence regions, are less suited for hydraulic applications but may enhance heat transfer by disrupting the thermal boundary layer, suggesting potential for cooling applications. However, to capture unsteady flow phenomena such as vortex shedding or transient eddy effects, future studies should employ large-eddy simulations.

4. Conclusion

This study examined the fluid dynamic effects of manufacturing-induced surface roughness in additively manufactured channels with self-supporting (droplet, diamond) and non-self-supporting (circular) cross-sections. An advanced parametric surface roughness model was proposed, based on Chahid et al. (2021). The numerical analyses conducted under laminar and turbulent flow conditions demonstrated that diamond cross-sections had significantly higher pressure losses than circular and droplet shapes of equal cross-sectional area. The impact of overhang-dependent surface roughness on AM channel designs was revealed through the analysis of pressure loss data, flow velocities, and turbulence intensities. Diamond cross-sections, which have been shown to promote turbulences the most, warrant further study to evaluate their potential benefits in heat transfer. In applications that prioritize minimal flow resistance,

https://doi.org/10.1017/pds.2025.10115 Published online by Cambridge University Press

such as AM-designed hydraulic components, droplet cross-sections are preferable due to their reduced pressure losses. It is notable that self-supporting cross-sections should be utilized exclusively within overhang regions, while circular shapes remain the optimal choice in other areas. In the future, research should focus on refining the roughness model approach to more accurately represent diverse surface characteristics in overhangs. To enhance the simulation model's precision, experimental investigations of the diamond and droplet channels is required in prospective studies.

References

Biedermann, M., Beutler, P., & Meboldt, M. (2022a). Automated Knowledge Based Design for Additive Manufacturing: A Case Study with Flow Manifolds. *Chemie Ingenieur Technik*. Advance online publication. https://doi.org/10.1002/cite.202100209

Biedermann, M., Beutler, P., & Meboldt, M. (2022b). Routing multiple flow channels for additive manufactured parts using iterative cable simulation. *Additive Manufacturing*, 56. https://doi.org/10.1016/j.addma.2022.102891

Biedermann, M., & Meboldt, M. (2020). Computational design synthesis of additive manufactured multi-flow nozzles. *Additive Manufacturing*, 35. https://doi.org/10.1016/j.addma.2020.101231

Brkić, D. (2011). Review of explicit approximations to the Colebrook relation for flow friction. *Journal of Petroleum Science and Engineering*, 77 (1), 34–48. https://doi.org/10.1016/j.petrol.2011.02.006

Bulsiewicz, T., & Łapka, P. (2024). Effects of additive manufacturing on convective heat transfer in 3D-printed micro/mini-channels and fluid passages with micro/mini structures – The review. *International Communications in Heat and Mass Transfer*, 159. https://doi.org/10.1016/j.icheatmasstransfer.2024.108057

Chahid, Y., Racasan, R., Pagani, L., Townsend, A., Liu, A., Bills, P., & Blunt, L. (2021). Parametrically designed surface topography on CAD models of additively manufactured lattice structures for improved design validation. *Additive Manufacturing*, 37, 101731. https://doi.org/10.1016/j.addma.2020.101731

F42 Committee. (2019). *Additive manufacturing Design Part 1: Laser-based powder bed fusion of metals. (ISO/ASTM52911-1-19)*. ASTM International. https://www.astm.org/f3280-19.html

Garg, H., Wang, L., Sahut, G., & Fureby, C. (2023). Large eddy simulations of fully developed turbulent flows over additively manufactured rough surfaces. *Physics of Fluids*, 35 (4). https://doi.org/10.1063/5.0143863

Han, Q., Gu, H., Soe, S., Setchi, R., Lacan, F., & Hill, J. (2018). Manufacturability of AlSi10Mg overhang structures fabricated by laser powder bed fusion. *Materials and Design*, 160, 1080–1095. https://doi.org/10.1016/j.matdes.2018.10.043

Hartsfield, C. R., Shelton, T. E., Cobb, G. R., Kemnitz, R. A., & Weber, J. (2021). Understanding Flow Characteristics in Metal Additive Manufacturing. *Journal of Aerospace Engineering*, 34 (6). https://doi.org/10.1061/(ASCE)AS.1943-5525.0001325

Kasperovich, G., Becker, R., Artzt, K., Barriobero-Vila, P., Requena, G., & Haubrich, J. (2021). The effect of build direction and geometric optimization in laser powder bed fusion of Inconel 718 structures with internal channels. *Materials & Design*, 207. https://doi.org/10.1016/j.matdes.2021.109858

Lamarche-Gagnon, M.-É., Molavi-Zarandi, M., Raymond, V., & Ilinca, F. (2024). Additively manufactured conformal cooling channels through topology optimization. *Structural and Multidisciplinary Optimization*, 67 (8). https://doi.org/10.1007/s00158-024-03846-3

Perlin, K. (2002). Improving noise. *ACM Transactions on Graphics*, 21(3), 681–682.

Schmelzle, J., Kline, E. V., Dickman, C. J., Reutzel, E. W., Jones, G., & Simpson, T. W. (2015). (Re)Designing for Part Consolidation: Understanding the Challenges of Metal Additive Manufacturing. *Journal of Mechanical Design*, 137 (11). https://doi.org/10.1115/1.4031156

Schmitt, F., Sallehsari, K., & Kirchner, E. (2023). How to control the surface qualities in AM channels? In *DS 125: Proceedings of the 34th Symposium Design for X (DFX2023)* (pp. 153–162). The Design Society. https://doi.org/10.35199/dfx2023.16

Swamee, P. K. (1993). Design of a Submarine Oil Pipeline. *Journal of Transportation Engineering*, 119 (1), 159–170. https://doi.org/10.1061/(ASCE)0733-947X(1993)119:1(159)

Tappeiner, Z., Donners, M., Schmid, M., & Schmitz, K. (2024). ADDITIVE MANUFACTURING OF HYDRAULIC COMPONENTS - PRESSURE LOSS COMPARISON OF DIFFERENT SELF-SUPPORTING CHANNEL GEOMETRIES. In P. D.-I. J. Weber (Ed.), *14th International Fluid Power Conference* (pp. 267–280). River Publishers. https://doi.org/10.13052/rp-9788770042222C20

Wildgoose, A. J., & Thole, K. A. (2023). Heat Transfer and Pressure Loss of Additively Manufactured Internal Cooling Channels With Various Shapes. *Journal of Turbomachinery*, 145 (7). https://doi.org/10.1115/1.4056775

Zhang, C., Wang, S., Li, J., Zhu, Y., Peng, T., & Yang, H. (2020). Additive manufacturing of products with functional fluid channels: A review. *Additive Manufacturing*, 36. https://doi.org/10.1016/j.addma.2020.101490

https://doi.org/10.1017/pds.2025.10115 Published online by Cambridge University Press